Robust Power Flow Control of Grid-Connected Inverters

Yeqin Wang, *Student Member, IEEE*, Beibei Ren, *Member, IEEE*, and Qing-Chang Zhong, *Senior Member, IEEE*

***Abstract*—In this paper, an uncertainty and disturbance estimator (UDE)-based robust power flow control is developed for grid-connected inverters to achieve accurate power delivery to the grid. The model of power delivering with both frequency dynamics and voltage dynamics is derived at first. The UDE method is introduced into the controller design to deal with model uncertainties (e.g., output impedance and power angle), coupling effects, and external disturbances (e.g., the fluctuation of the dc-link voltage, the variation of output impedance/line impedance, and the variations of both frequency and amplitude in the grid voltage). Also, this controller does not need a voltage regulator or a current regulator and is easy for the implementation and parameter tuning through the design of the desired tracking error dynamics and the UDE filters. Experimental results are provided to show the effectiveness of the proposed method for different disturbance rejection scenarios, the low-voltage fault-ride through capability, and the weak grid operation capability. The good robustness of the UDE-based control is also demonstrated through the comparison with two other controllers: the proportional–integral controller and the active disturbance rejection controller.**

***Index Terms*—Fluctuation of dc-link voltage, grid disturbances, model uncertainties, uncertainty and disturbance estimator (UDE), variation of the impedance.**

I. Introduction

NOWADAYS, renewable energies play very important roles in energy area. Most of the renewable energies are comprised of variable-frequency ac sources (e.g., wind turbines), high-frequency ac sources (e.g., small gas turbines), or dc sources (e.g., solar photovoltaics). The dc/ac converters, also called grid-connected inverters (GCI), are needed to interface renewable energies with the public-utility grid [1]. Though renewable energies are quite popular, there are still some challenges faced by the GCI control for grid integration. For example, the renewable energies, such as wind power, solar photovoltaics, are unstable in changing wind conditions or sunlight conditions; the variations of the grid voltage (frequency variation, phase variation, or amplitude variation), even though they are small, affect the stability of the GCI and grid operation; and the fluctuating dc-link voltage also often affects the GCI control for renewable energies [2], [3].

The vector control, originally proposed for the control of electrical machine drive systems [4], is a popular control algorithm for three-phase GCI to convert dc power to ac power [5]–[7]. In the vector control, the current regulation in the dq reference frame is adopted to generate voltage reference control signals. An extra synchronization unit, e.g., the phase-locked loop (PLL), is required for the transformations of both current and voltage between the abc reference frame and the dq reference frame. However, the vector control has its fundamental limitations in the grid voltage variation conditions. First, the frequency dynamics are not considered in the vector control, which makes it difficult to analyze the power angle and frequency stability between the GCI and the grid [3]. Second, the PLL dynamics can affect the stability of the GCI, particularly in weak grids [3], [8]–[10], and the control response is also limited by the response of PLL [11], [12]. Third, the variation of the dc-link dynamics can also affect the stability of the GCI in the vector control [3]. Moreover, because the PLL is inherently nonlinear and so are the inverter controller and the power system, it is extremely difficult and time-consuming to tune the PLL parameters to achieve a satisfactory performance [12].

The droop control method for power sharing among parallel-operated inverters [13] can be adopted for the GCI to achieve power flow control [14]–[18]. Though some merits are achieved with the droop control method, such as the harmonic current regulation [14], flexible operation in either grid-connected mode or islanded mode [15], [17], and enhancing power loop dynamics [16], the extra synchronization units are still needed in most cases [14], [16]–[18]. It still has limitations for the droop control method to deal with variations of the grid voltage, and extra control loops (a voltage regulator or a current regulator) [11] are required to combine with the droop control method [14], [15], [17], [18].

Inverters also can be controlled to behave as virtual synchronous machines (VSM) [19], [20]. The self-tuning algorithms for optimal parameters of the VSM are studied in [21]; however, the PLL is still needed in this method. Similar to the synchronization mechanism of a synchronous machine, a power-synchronization control is proposed for voltage-source converters in [22] without the needs of PLL. Following the work on the synchronverter technology [20], a dedicated synchronization unit is completely removed in [12]. The similar

Manuscript received January 20, 2016; revised May 1, 2016; accepted May 14, 2016. Date of publication June 29, 2016; date of current version October 7, 2016. This work was supported in part by the National Science Foundation under Grant DGE-1438921.

Y. Wang is with the National Wind Institute, Texas Tech University, Lubbock, TX 79409-1021 USA (e-mail: yeqin.wang@ttu.edu).

B. Ren is with the Department of Mechanical Engineering, Texas Tech University, Lubbock, TX 79409-1021 USA (e-mail: beibei.ren@ttu.edu).

Q.-C. Zhong is with the Department of Electrical and Computer Engineering, Illinois Institute of Technology, Chicago, IL 60616 USA (e-mail: zhongqc@ieee.org).

Color versions of one or more of the figures in this paper are available online at http://ieeexplore.ieee.org.

Digital Object Identifier 10.1109/TIE.2016.2586439

concept of the VSM is expanded to introduce the inertia to the grid [3] and to improve the microgrid's stability [9] without a synchronization unit.

In this paper, a robust power flow control strategy based on the uncertainty and disturbance estimator (UDE) method is developed for GCI to deliver both real power and reactive power to the utility grid. The UDE control algorithm, which was first proposed in [23], is based on an assumption that the uncertainty and disturbance can be estimated by using a filter with an appropriate bandwidth. In recent years, the UDE-based control demonstrates its excellent robust performances in different applications, such as robust trajectory tracking [24], control for a class of nonaffine nonlinear systems [25], and the variable-speed wind turbine control [26]. In this paper, the model of power delivering with both frequency dynamics and voltage dynamics is derived at first. Then, the UDE method is introduced into the controller design to achieve accurate regulation of both real power and reactive power, in the presence of the model uncertainties (e.g., output impedance and power angle), the coupling effects, and the external disturbances (e.g., the fluctuation of dc-link voltage, variation of output impedance/line impedance, and variations of the grid voltage). Also, this controller does not require an extra synchronization unit in grid-connected operation, apart from an initial synchronization. This approach has a simple structure without either voltage regulation or current regulation and is easy for the implementation and parameter tuning with the design of the desired tracking error dynamics and the UDE filters. The effectiveness of the proposed control approach is investigated by theoretical analysis and demonstrated through experimental studies on an experimental test rig. Though this method is developed based on single-phase GCI in this paper, the results can be further extended to three-phase GCI. With the capability of handling the variations of the grid voltage, the UDE-based robust power flow control is suitable for weak grids. Also with the individual control of the real power and reactive power, this approach can be extended to other applications, such as static synchronous compensators and active power filters.

The rest of this paper is organized as follows. Section II provides the dynamics of power delivery. In Section III, the UDE-based robust power flow control is proposed for the GCI. Both stability analysis and steady-state performance analysis are provided. The effectiveness of the proposed approach is demonstrated through the experimental validation in Section IV, with the concluding remarks made in Section V.

II. Dynamics of Power Delivery

A voltage source $E\angle\delta$ delivering power to the grid $V_o\angle 0^\circ$ through an impedance $Z\angle\theta$ can be modeled in Fig. 1. The real power P and the reactive power Q received by the grid $V_o\angle 0^\circ$ can be obtained as [1]

$$P = \left(\frac{EV_o}{Z}\cos\delta - \frac{V_o^2}{Z}\right)\cos\theta + \frac{EV_o}{Z}\sin\delta\sin\theta \quad (1)$$

$$Q = \left(\frac{EV_o}{Z}\cos\delta - \frac{V_o^2}{Z}\right)\sin\theta - \frac{EV_o}{Z}\sin\delta\cos\theta \quad (2)$$

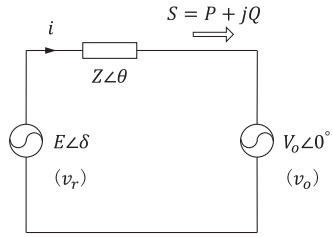

Fig. 1. Voltage source delivering power to the grid.

where δ is the phase difference between the voltage source and the grid, often called the power angle. Here, the grid voltage v_o is used as the reference, with the initial angle of grid voltage defined as zero.

Taking the derivatives of both (1) and (2), the dynamics of power delivery are expressed in

$$\dot{P} = \frac{EV_o\dot{\delta}}{Z}\cos\delta\sin\theta - \frac{EV_o\dot{\delta}}{Z}\sin\delta\cos\theta + \frac{V_o\dot{E}}{Z}\cos\delta\cos\theta + \frac{V_o\dot{E}}{Z}\sin\delta\sin\theta \quad (3)$$

$$\dot{Q} = \frac{V_o\dot{E}}{Z}\cos\delta\sin\theta - \frac{EV_o\dot{\delta}}{Z}\sin\delta\sin\theta - \frac{EV_o\dot{\delta}}{Z}\cos\delta\cos\theta - \frac{V_o\dot{E}}{Z}\sin\delta\cos\theta. \quad (4)$$

Since the power angle δ depends on the output power of the GCI, and the output impedance $Z\angle\theta$ always drifts with the changes of environments (e.g., inductance change with magnetic saturation caused by high current, and resistance change by high temperature), they are quite uncertain. Moreover, nonlinear and coupling terms, e.g., $\frac{V_o\dot{E}}{Z}\sin\delta\sin\theta$ and $\frac{V_o\dot{E}}{Z}\sin\delta\sin\theta$, exist in the dynamics of real power (3), and $\frac{EV_o\dot{\delta}}{Z}\sin\delta\sin\theta$ and $\frac{EV_o\dot{\delta}}{Z}\cos\delta\cos\theta$ exist in the dynamics of reactive power (4). The uncertainties, the nonlinearity, and the coupling effects cause difficulties for control design of power delivery.

For the GCI, similar to the winding inductance in synchronous generators, because of the output LC filters or the inductance of line impedance, the output impedance is mostly inductive. It means $\sin\theta \approx 1$ and $\cos\theta \approx 0$ with $\theta \approx 90^\circ$. In practice, the power angle δ is usually very small with $\sin\delta \approx 0$ and $\cos\delta \approx 1$. Then, the dynamics of power delivery (3) and (4) can be rewritten as

$$\dot{P} = \frac{EV_o}{Z_o}\dot{\delta} + \triangle_p \quad (5)$$

$$\dot{Q} = \frac{V_o}{Z_o}\dot{E} + \triangle_q \quad (6)$$

where

$$\triangle_p = \frac{EV_o\dot{\delta}}{Z_o}(\cos\delta\sin\theta - 1) - \frac{EV_o\dot{\delta}}{Z_o}\sin\delta\cos\theta + \frac{V_o\dot{E}}{Z_o}\cos\delta\cos\theta + \frac{V_o\dot{E}}{Z_o}\sin\delta\sin\theta + d_{\text{pzo}} \quad (7)$$

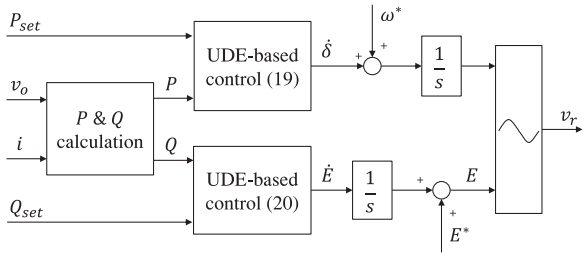

Fig. 2. UDE-based robust power flow control.

$$\begin{aligned}\triangle_q &= \frac{V_o\dot{E}}{Z_o}(\cos\delta\sin\theta - 1) - \frac{EV_o\dot{\delta}}{Z_o}\sin\delta\sin\theta \\ &= -\frac{EV_o\dot{\delta}}{Z_o}\cos\delta\cos\theta - \frac{V_o\dot{E}}{Z_o}\sin\delta\cos\theta + d_{\text{qzo}} \quad (8)\end{aligned}$$

represent the lumped uncertain terms, including the uncertainties, the nonlinearity, and the coupling effects. d_{pzo} and d_{qzo} are the deviations due to the deviation of the real output impedance Z in (3) and (4) from the nominal output impedance Z_o. In practice, the lumped uncertain terms $\triangle_p$ and $\triangle_q$ can be small and bounded because of the inductive output impedance and small power angle δ in GCI. With the treatment based on the uncertain terms (7) and (8), the dynamics of power delivery (3) and (4) are reduced as linear equations in (5) and (6) plus the uncertain terms, which will simplify the following controller design. Also, the uncertain terms $\triangle_p$ and $\triangle_q$ will be estimated and compensated in the following controller design.

III. Robust Power Flow Control

In this section, an UDE-based robust power flow control is developed for the GCI based on the dynamics of power delivery (5) and (6). The structure is shown in Fig. 2. The real power and reactive power can be regulated individually.

A. Controller Design

The inverter should deliver both real power and reactive power to the grid accurately. The control objective is to achieve the regulations of both real power and reactive power, such that the real power P and the reactive power Q asymptotically track their settings P_{set} and Q_{set}, respectively. In particular, the tracking errors

$$e_p = P_{\text{set}} - P \quad \text{and} \quad e_q = Q_{\text{set}} - Q$$

should satisfy the error dynamic equations

$$\dot{e}_p = -K_p e_p \quad (9)$$

$$\dot{e}_q = -K_q e_q \quad (10)$$

where $K_p > 0$ and $K_q > 0$ are the constant error feedback gains.

Combining (5) and (9) and (6) and (10), respectively, then

$$\dot{P}_{\text{set}} - \frac{EV_o}{Z_o}\dot{\delta} - \triangle_p = -K_p e_p \quad (11)$$

$$\dot{Q}_{\text{set}} - \frac{V_o}{Z_o}\dot{E} - \triangle_q = -K_q e_q. \quad (12)$$

Therefore, $\dot{\delta}$ and $\dot{E}$ need to satisfy

$$\dot{\delta} = \frac{Z_o}{EV_o}\left(\dot{P}_{\text{set}} - \triangle_p + K_p e_p\right) \quad (13)$$

$$\dot{E} = \frac{Z_o}{V_o}\left(\dot{Q}_{\text{set}} - \triangle_q + K_q e_q\right). \quad (14)$$

According to the system dynamics in (5) and (6), the uncertain terms $\triangle_p$ and $\triangle_q$ can be obtained as

$$\triangle_p = \dot{P} - \frac{EV_o}{Z_o}\dot{\delta}, \quad \triangle_q = \dot{Q} - \frac{V_o}{Z_o}\dot{E}.$$

Following the procedures of the UDE design provided in [23], $\triangle_p$ and $\triangle_q$ can be estimated by

$$\hat{\triangle}_p = (\dot{P} - \frac{EV_o}{Z_o}\dot{\delta}) * g_{\text{pf}} \quad (15)$$

$$\hat{\triangle}_q = (\dot{Q} - \frac{V_o}{Z_o}\dot{E}) * g_{\text{qf}} \quad (16)$$

where "$*$" is the convolution operator, and $g_{\text{pf}}(t)$ and $g_{\text{qf}}(t)$ are the impulse response of strictly proper stable filters $G_{\text{pf}}(s)$ and $G_{\text{qf}}(s)$ with the appropriate bandwidth. Replacing $\triangle_p$ and $\triangle_q$ with $\hat{\triangle}_p$ and $\hat{\triangle}_q$ in (13) and (14) results in

$$\dot{\delta} = \frac{Z_o}{EV_o}\left[\dot{P}_{\text{set}} + K_p e_p - (\dot{P} - \frac{EV_o}{Z_o}\dot{\delta}) * g_{\text{pf}}\right] \quad (17)$$

$$\dot{E} = \frac{Z_o}{V_o}\left[\dot{Q}_{\text{set}} + K_q e_q - (\dot{Q} - \frac{V_o}{Z_o}\dot{E}) * g_{\text{qf}}\right]. \quad (18)$$

Furthermore, the UDE-based robust power flow control laws are obtained as

$$\begin{aligned}\dot{\delta} = \frac{Z_o}{EV_o}\Bigg[&L^{-1}\left\{\frac{1}{1-G_{\text{pf}}(s)}\right\} * (\dot{P}_{\text{set}} + K_p e_p) \\ &- L^{-1}\left\{\frac{sG_{\text{pf}}(s)}{1-G_{\text{pf}}(s)}\right\} * P\Bigg] \quad (19)\end{aligned}$$

$$\begin{aligned}\dot{E} = \frac{Z_o}{V_o}\Bigg[&L^{-1}\left\{\frac{1}{1-G_{\text{qf}}(s)}\right\} * (\dot{Q}_{\text{set}} + K_q e_q) \\ &- L^{-1}\left\{\frac{sG_{\text{qf}}(s)}{1-G_{\text{qf}}(s)}\right\} * Q\Bigg]. \quad (20)\end{aligned}$$

The final controller output v_r for generating pulse width modulation (PWM) signals can be obtained after combining the frequency from the phase δ and the amplitude obtained from E, as shown in Fig. 2, where ω^* is the rated frequency and E^* is the rated voltage for global settings. Here, V_o can be the denominator in both (19) and (20), since the amplitude of the grid voltage V_o is nonzero.

It is worth noting that the uncertain terms $\triangle_p$ (7) and $\triangle_q$ (8) include the model uncertainties of the output impedance $Z\angle\theta$ and the power angle δ for the GCI. The variation of output impedance (e.g., caused by high current, or by high temperature), the addition of virtual impedance, and the change of power angle can be estimated and compensated by the UDE-based control algorithms (19) and (20).

The grid voltage v_o and the output current i of the GCI are measured to calculate the real power P and the reactive power Q,

as shown in Fig. 2, so that the real power and reactive power can be controlled individually. The GCI with the UDE-based robust power flow control can regulate its own frequency and voltage based on the tracking errors of the real power e_p and the reactive power e_q. When the disturbances happen in the grid voltage (e.g., variations of frequency or amplitude), the power outputs P and Q will change from the reference values P_{set} and Q_{set}, which causes the proposed controller to regulate the frequency and voltage of the GCI till both power output tracking errors converge to zero. Therefore, the UDE-based robust power flow control can deal with the variations of both frequency and amplitude in the grid voltage without an extra synchronization unit for the grid-connected operation. The change of line impedance will affect the measured grid voltage and the power outputs P and Q. This effect also can be compensated by the UDE-based controller.

Furthermore, a PWM modulation unit is applied in the controller output v_r, as shown in Fig. 2, to convert the dc voltage to the ac voltage. This might introduce the disturbances of the fluctuating dc-link voltage into the system. The fluctuating dc-link voltage also can be treated as external disturbances and handled by the UDE-based robust power flow control (19) and (20). There is no requirement to measure the dc-link voltage, as long as the dc-link voltage is high enough to deliver power to the grid. In practice, the dc-link voltage can be measured for other purposes, such as the protection.

In addition, an inner-current-loop control can be added to the controller output v_r shown in Fig. 2 for other purposes, such as the virtual impedance design [27] and the current protection [1]. However, the added virtual impedance will not affect the performance of power delivery with the proposed method. The related experimental result will be shown in Section IV.

B. Stability Analysis

Theorem 1. Considering the GCI delivering power to the grid with the dynamics (5) and (6), and the UDE-based robust power flow control laws (19) and (20), if the lumped uncertain terms $\triangle_p$ (7) and $\triangle_q$ (8) are bounded, then the closed-loop system is stable in the sense of boundedness, i.e., the power-tracking errors e_p and e_q are bounded for all $t \geq 0$.

Proof. Considering the Lyapunov function candidate

$$V(t) = \frac{1}{2}(e_p^2 + e_q^2).$$

Taking the derivative of $V(t)$, along with (9)–(12),

$$\begin{aligned}\dot{V}(t) =& \; e_p\dot{e}_p + e_q\dot{e}_q \\ =& \; e_p\left(\dot{P}_{\text{set}} - \frac{EV_o}{Z_o}\dot{\delta} - \triangle_p\right) \\ &+e_q\left(\dot{Q}_{\text{set}} - \frac{V_o}{Z_o}\dot{E} - \triangle_q\right).\end{aligned}$$

With the UDE-based control laws (19) and (20), and along with (15) and (16),

$$\begin{aligned}\dot{V}(t) =& \; e_p\left(-K_p e_p + \hat{\triangle}_p - \triangle_p\right) \\ &+e_q\left(-K_q e_q + \hat{\triangle}_q - \triangle_q\right) \\ =& \; -K_p e_p^2 - K_q e_q^2 - e_p\tilde{\triangle}_p - e_q\tilde{\triangle}_q \end{aligned} \tag{21}$$

where $\tilde{\triangle}_p \triangleq \triangle_p - \hat{\triangle}_p$ and $\tilde{\triangle}_q \triangleq \triangle_q - \hat{\triangle}_q$ are the estimated errors of the uncertain terms. According to (15) and (16), the estimated errors are represented as

$$\tilde{\triangle}_p = \triangle_p * L^{-1}\left\{1 - G_{\text{pf}}(s)\right\} \tag{22}$$

$$\tilde{\triangle}_q = \triangle_q * L^{-1}\left\{1 - G_{\text{qf}}(s)\right\}. \tag{23}$$

Since the filters $G_{\text{pf}}(s)$ and $G_{\text{qf}}(s)$ are strictly proper stable filters with the appropriate bandwidth, if the lumped uncertain terms $\triangle_p$ (7) and $\triangle_q$ (8) are bounded, the estimated errors $\tilde{\triangle}_p$ and $\tilde{\triangle}_q$ are bounded. By applying Young's inequality to (21), there is

$$\begin{aligned}\dot{V}(t) \leq& \; -K_p e_p^2 - K_q e_q^2 + \frac{1}{2}e_p^2 + \frac{1}{2}\tilde{\triangle}_p^2 + \frac{1}{2}e_q^2 + \frac{1}{2}\tilde{\triangle}_q^2 \\ =& \; -\left(K_p - \frac{1}{2}\right)e_p^2 - \left(K_q - \frac{1}{2}\right)e_q^2 \\ &+\frac{1}{2}\tilde{\triangle}_p^2 + \frac{1}{2}\tilde{\triangle}_q^2 \\ \leq& \; -c_1 V(t) + c_2 \end{aligned} \tag{24}$$

where $c_1 = \min\{2K_p - 1,\, 2K_q - 1\} > 0$, and $c_2 \geq 0$ is the upper bound for $\frac{1}{2}\tilde{\triangle}_p^2 + \frac{1}{2}\tilde{\triangle}_q^2$. Then, solving (24) gives

$$0 \leq V(t) \leq V(0)e^{-c_1 t} + \frac{c_2}{c_1}(1 - e^{-c_1 t}) \tag{25}$$

where $V(0) = \frac{1}{2}\left[e_p^2(0) + e_q^2(0)\right]$ is the initial value. When $t \to \infty$, the first term on the right-hand side of (25) will decay to 0, and the second term is bounded with $\frac{c_2}{c_1}$. This means $V(t)$ is bounded for all $t \geq 0$. Therefore, the closed-loop system is stable in the sense of boundedness, which indicates that the power-tracking errors e_p and e_q are bounded for all $t \geq 0$.

The bounds of e_p and e_q can be adjusted through the design of feedback gains K_p, K_q and the filters $G_{\text{pf}}(s)$ and $G_{\text{qf}}(s)$. When the estimations of the uncertain terms $\triangle_p$ and $\triangle_q$ are accurate enough, e.g., the filters $G_{\text{pf}}(s)$ and $G_{\text{qf}}(s)$ have the unity gain over the bandwidths of $\triangle_p$ and $\triangle_q$, respectively, the estimation errors $\tilde{\triangle}_p$ and $\tilde{\triangle}_q$ will be close to zero. Then, the power-tracking errors e_p and e_q will converge to zero.

C. Steady-State Performance

The steady-state performance of power delivery for the GCI will be analyzed in this section.

When the estimated terms $\hat{\triangle}_p$ (15) and $\hat{\triangle}_q$ (16) are adopted to replace $\triangle_p$ in (13) and $\triangle_q$ in (14), the error dynamics (9) and

(10) become

$$\begin{aligned}\dot{e}_p &= -K_p e_p - (\triangle_p - \hat{\triangle}_p) \\ &= -K_p e_p - \tilde{\triangle}_p \qquad (26)\\ \dot{e}_q &= -K_q e_q - (\triangle_q - \hat{\triangle}_q) \\ &= -K_q e_q - \tilde{\triangle}_q. \qquad (27)\end{aligned}$$

By substituting (22) into (26), substituting (23) into (27), and taking the Laplace transformation

$$sE_p(s) = -K_p E_p(s) - \blacktriangle_p(s)\,[1 - G_{\rm pf}(s)] \qquad (28)$$

$$sE_q(s) = -K_q E_q(s) - \blacktriangle_q(s)\,[1 - G_{\rm qf}(s)] \qquad (29)$$

where $E_p(s)$, $\blacktriangle_p(s)$, $E_q(s)$, and $\blacktriangle_q(s)$ are the Laplace transform of e_p, $\triangle_p$, e_q, and $\triangle_q$, respectively. Then

$$E_p(s) = -\frac{\blacktriangle_p(s)\,[1 - G_{\rm pf}(s)]}{s + K_p} \qquad (30)$$

$$E_q(s) = -\frac{\blacktriangle_q(s)\,[1 - G_{\rm qf}(s)]}{s + K_q}. \qquad (31)$$

It is worth noting that $\triangle_p$ in (7) and $\triangle_q$ in (8) are normally small with the small power angle δ and inductive output impedance. They can be assumed bounded, i.e.,

$$\lim_{s\to 0} s \cdot \blacktriangle_p(s) < \infty, \ \lim_{s\to 0} s \cdot \blacktriangle_q(s) < \infty.$$

If the filters $G_{\rm pf}(s)$ and $G_{\rm qf}(s)$ are designed as the strictly-proper stable filters with $G_{\rm pf}(0) = 1$ and $G_{\rm qf}(0) = 1$, by applying the final value theorem to (30) and (31), there are

$$\begin{aligned}\lim_{t\to\infty} e_p &= \lim_{s\to 0} s \cdot E_p(s) \\ &= -\lim_{s\to 0} \frac{s \cdot \blacktriangle_p(s)\,[1 - G_{\rm pf}(s)]}{s + K_p} \\ &= 0 \\ \lim_{t\to\infty} e_q &= \lim_{s\to 0} s \cdot E_q(s) \\ &= -\lim_{s\to 0} \frac{s \cdot \blacktriangle_q(s)\,[1 - G_{\rm qf}(s)]}{s + K_q} \\ &= 0.\end{aligned}$$

Hence, the mean values of tracking errors for both real power and reactive power converge to zero and accurate power delivery to the grid is achieved.

IV. Experimental Validation

A. Experimental Setup

Although the major uncertainties and disturbances are considered in the theoretical development, some practical issues cannot be fully considered. In order to verify the real-time performance of the UDE-based robust power flow control (19) and (20), a test rig with one experimental inverter delivering power to a simulated grid provided by a controlled inverter shown in Fig. 3(a) is built up. The circuit diagram is shown in Fig. 3(b), where a load consisting of a resistor $R_L = 40\ \Omega$ and a capacitor $C_L = 45\ \mu$F is connected to the controlled inverter to provide the base power consumption. The experimental inverter is connected to the grid simulator via a switch $CB1$ and a line resistance $R_{\rm line} = 2\ \Omega$. The line resistance $R_{\rm line}$ is bypassed by a switch $CB2$ to mimic the change of line impedance. The inverter parameters are given in Table I. Here, the impedance of experimental inverter includes the parasitic resistance and the filter capacitor. As mentioned earlier, these effects can be dealt with by the proposed controller. The PWM frequency for power electronic devices is set as 19.2 kHz for both inverters. Both inverters are controlled through the Texas Instruments controlCARD with F28M35H52C1 microcontroller unit.

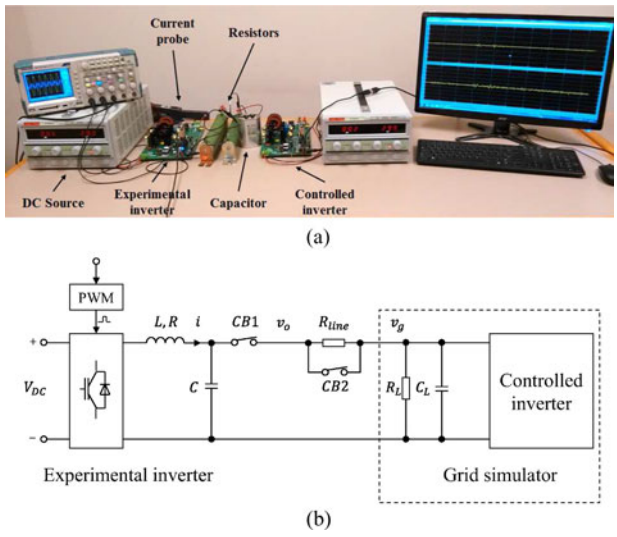

Fig. 3. Experimental test rig. (a) Setup. (b) Circuit diagram.

TABLE I
NOMINAL VALUES OF INVERTER PARAMETERS

Parameters	Values	Parameters	Values
L	7 mH	Grid voltage	110 $V_{\rm rms}$
R	1 Ω	Grid frequency	60 Hz
C	1 μF	DC-link voltage	300 $V_{\rm DC}$

B. Selection of Control Parameters

The guidance of the parameters selection in the UDE-based robust power flow control (19) and (20) is provided as follows. The constant feedback gains are chosen with $K_p = K_q = 20$ to achieve the desired tracking error dynamics. Then, $\frac{1}{K_p}$ and $\frac{1}{K_q}$ are time constants for the step response. The UDE filters $G_{\rm pf}(s)$ and $G_{\rm qf}(s)$ in (19) and (20) are chosen as the following second-order low-pass filters:

$$G_{\rm pf}(s) = \frac{\omega_p^2}{s^2 + \frac{\omega_p}{Q_p}s + \omega_p^2}, \quad G_{\rm qf}(s) = \frac{\omega_q^2}{s^2 + \frac{\omega_q}{Q_q}s + \omega_q^2}.$$

In order to get a better estimation of uncertain terms $\triangle_p$ and $\triangle_q$ and achieve the desired tracking error dynamics, the bandwidths of UDE filters $G_{\rm pf}(s)$ and $G_{\rm qf}(s)$ should be bigger than the bandwidths of the desired step response, K_p and K_q, respectively, and wide enough to cover the spectrum of the lumped

uncertain terms $\triangle_p$ and $\triangle_q$. The filters parameters are chosen as $\omega_p = \omega_q = 25.1$, $Q_p = Q_q = 1$.

C. System Performance

1) With DC-Link Voltage Disturbances and Impedance Disturbances: In this scenario, the grid voltage and frequency are kept in nominal value. Three types of disturbances, i.e., change of dc-link voltage, addition of virtual impedance, and change of line impedance, are considered.

First, the change of dc-link voltage is studied. Initially, the switch $CB1$ is OFF and switch $CB2$ is ON. The simulated grid is set with the nominal frequency 60 Hz and the nominal voltage 110 Vrms. The grid simulator is continuously working during the whole experimental test through the controlled inverter. The experimental inverter starts at $t = 0$ s. Then, the voltage v_o after $CB1$ is measured by the experimental inverter for the initial synchronization using the zero-crossing method [1] before $t = 3$ s. Therefore, the first 3 s are omitted from the plots. The initial synchronization is disabled after the experimental inverter is connected to the simulated grid with switch $CB1$ ON. The initial values of P_{set} and Q_{set} are set to zero. Then, we have the following.

1) The real power $P_{\text{set}} = 200$ W and the reactive power $Q_{\text{set}} = -100$ Var are applied at $t = 5$ s.

2) The real power P_{set} changes to 100 W at $t = 10$ s, and the reactive power Q_{set} changes to -50 Var at $t = 15$ s.

3) The dc-link voltage of the experimental inverter changes from 299 to 270 V_{DC} at $t = 20$ s and returns to 299 V_{DC} at $t = 25$ s.

4) The test is stopped at $t = 30$ s.

The same initial settings and step 1 are also applied in other cases.

The system responses are shown in the left column of Fig. 4. After the experimental inverter is connected to the grid simulator, the real power and reactive power remain at zero. After $t = 5$ s, the real power and reactive power reach the set points with $P = 200$ W in Fig. 4(a) and $Q = -100$ Var in Fig. 4(c) within 0.5 s, and the overshoots are almost zero. The change of real power causes a positive spike in the inverter frequency, as shown in Fig. 4(b), since the experimental inverter should generate a phase-lead to increase the power delivered to the simulated grid. Then, the inverter frequency settles down quickly. The real power and reactive power also have fast responses (within 0.5 s) with the set-point changes at $t = 10$ s and $t = 15$ s, respectively. The inverter frequency has a negative spike in the set-point change of real power with the similar reason as mentioned earlier. The changes of voltage E, though are very small before $t = 20$ s, exist in different power settings, as shown in Fig. 4(d), in order to meet the desired power references. When the dc-link voltage changes at both $t = 20$ s and $t = 25$ s, as shown in Fig. 4(e), the real power and reactive power keep almost unchanged, but the voltage E changes by about 10%, as shown in Fig. 4(d), to compensate the changes of the dc-link voltage (about 10%). The response of the voltage E is not fast (about 2 s), because the changes of the dc-link voltage are not fast either.

Second, the addition of virtual impedance is studied. The real power $P_{\text{set}} = 200$ W and the reactive power $Q_{\text{set}} = -100$ Var are still applied at $t = 5$ s. A virtual impedance $R_v = 2\,\Omega$ with feedback current is added at $t = 10$ s and then removed at $t = 20$ s to mimic the variation of output impedance. The system responses are shown in the middle column of Fig. 4. Though the reactive power has some big spikes (about 20%) after both $t = 10$ s and $t = 20$ s, it converges to the set point quickly (about 0.5 s). The inverter voltage E goes up with the effect of adding virtual impedance. The real power and the inverter frequency only have small spikes with adding and removing of virtual impedance, and settle down quickly.

Third, the change of line impedance is studied with Switch $CB2$ ON at $t = 10$ s and then OFF at $t = 20$ s. The system responses are almost same with the case of virtual impedance disturbances, as shown in the right column of Fig. 4. For the UDE-based control (19) and (20), the effects of virtual impedance disturbances and line impedance disturbances are similar with almost same voltage E, when $R_v = R_{\text{line}}$; however, the real output voltages of the experimental inverter are different for these two types of disturbances.

From the studies of this scenario, it can be seen that the UDE-based robust power flow control can achieve fast response with different desired power settings, where the real power and reactive power can be controlled individually in the presence of the coupling effects. The controller does not need a continuous synchronization unit after the experimental inverter is connected to the grid with an initial synchronization. At the same time, this UDE-based robust power flow control can reject the disturbances from the fluctuating dc-link voltage, the variation of output impedance, the addition/removing of virtual impedance, and the change of line impedance.

2) With Grid Disturbances: In this scenario, three types of grid disturbances are considered, i.e., step change of grid frequency, low-voltage fault-ride through, and connection with a weak grid. For the change of grid frequency and the low-voltage fault-ride through, they are achieved through the direct voltage and frequency control of the controlled inverter. For the connection with a weak grid, the droop control is applied in the controlled inverter to provide the frequency and voltage support for the simulated grid, functioning as a weak grid for the experimental inverter.

First, the change of grid frequency is considered. The simulated grid is initially set at the nominal frequency 60 Hz and nominal voltage 110 Vrms. With the same initial synchronization and power settings as previous scenario, we have the following.

1) The real power $P_{\text{set}} = 200$ W and the reactive power $Q_{\text{set}} = -100$ Var are applied at $t = 5$ s.
2) The grid frequency increases by 0.25 Hz at $t = 10$ s, and returns to normal 60 Hz at $t = 15$ s.
3) At $t = 20$ s, the grid frequency drops by 0.25 Hz, and returns to normal 60 Hz again at $t = 25$ s.
4) The test is stopped at $t = 30$ s.

The system responses are shown in the left column of Fig. 5. After $t = 10$ s, the real power is regulated well with some spikes

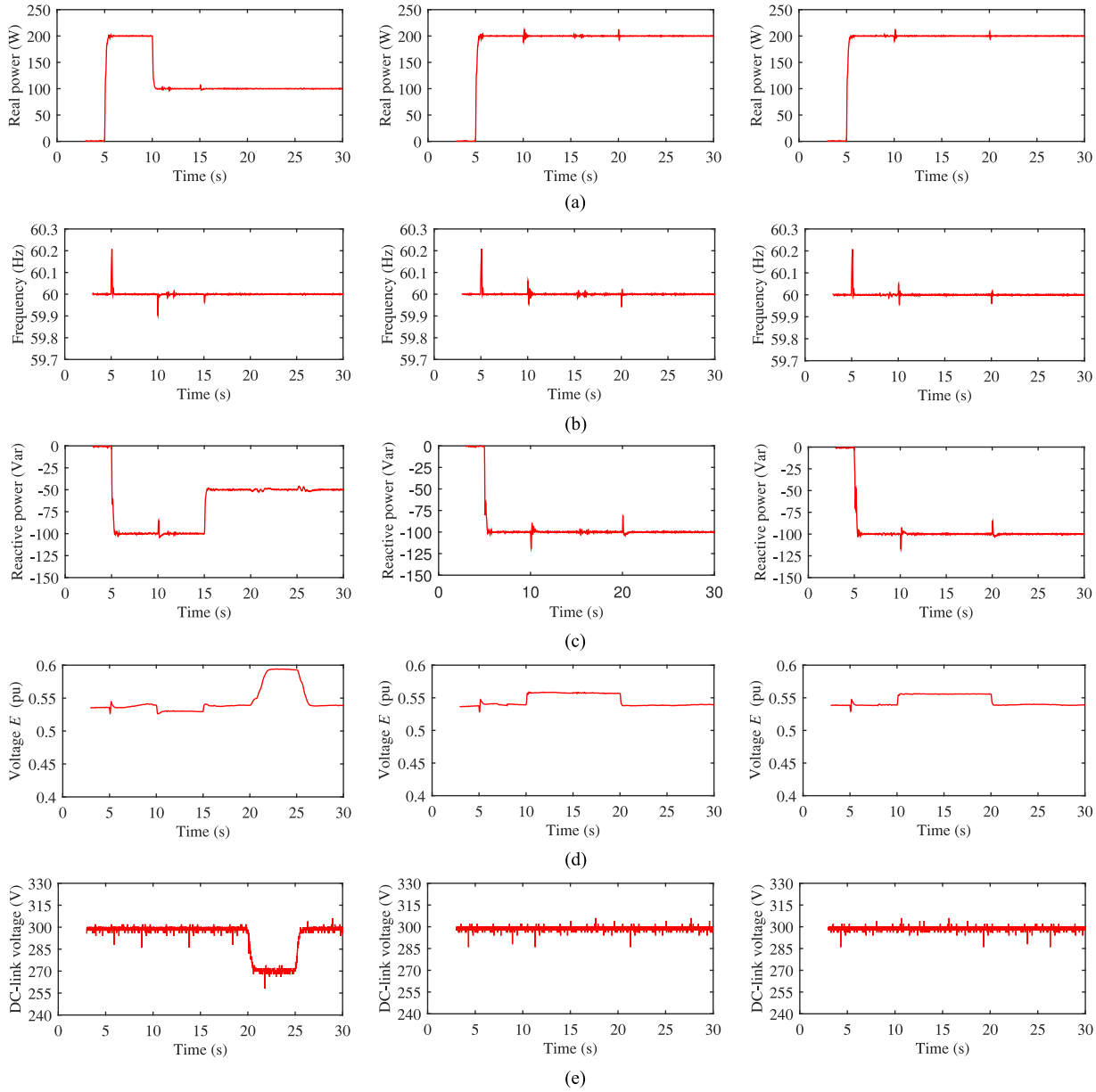

Fig. 4. Experimental results for dc-link voltage disturbances and impedance disturbances: change of dc-link voltage (left column), addition of virtual impedance (middle column), and change of line impedance (right column). (a) Real power. (b) Inverter frequency. (c) Reactive power. (d) Voltage E. (e) DC-link voltage.

(about 15%) when the grid frequency changes. The inverter frequency tracks the variation of the grid frequency well in each step change of the grid frequency. The reactive power and the voltage E keep almost unchanged when the grid frequency changes.

Second, the low-voltage fault-ride through is considered. The grid voltage increases by 10% at $t = 10$ s and returns to normal at $t = 15$ s; then, the grid voltage drops by 20% at $t = 20$ s and returns to normal again at $t = 25$ s. Here, the 20% drop of grid voltage is considered as a low-voltage fault condition. The system responses are shown in the middle column of Fig. 5. After $t = 10$ s, though the reactive power has some big spikes (about $\pm 20\%$ of spikes in 10% changes of grid voltage, about $\pm 25\%$ of spikes in 20% changes of grid voltage), it converges to the set point quickly (less than 0.8 s). The inverter voltage E tracks the amplitude variation of the grid voltage well in each step change. Though the real power and the inverter frequency have some spikes in the step changes of grid voltage, they settle down quickly. These spikes in both real power and inverter frequency are caused by the coupling effects. The related grid voltage is shown in Fig. 5(e).

Third, following the droop method in [28], the droop control with voltage droop coefficient $n = 0.036$ and frequency droop coefficient $m = 0.0006\,\pi$ is applied in the controlled inverter to

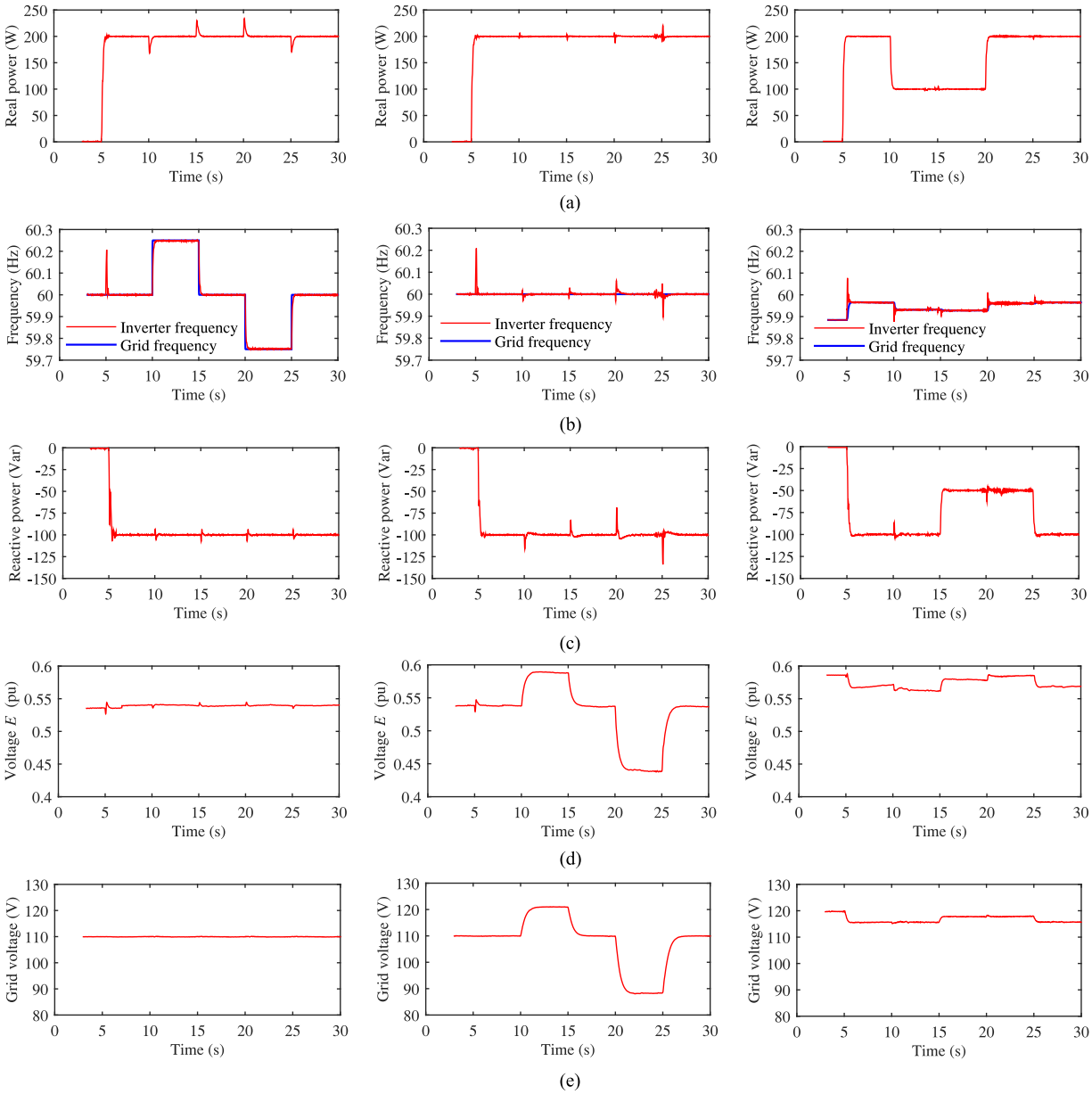

Fig. 5. Experimental results for the grid disturbances: change of the grid frequency (left column), low-voltage fault-ride through (middle column), and connection with a weak grid (right column). (a) Real power. (b) Inverter frequency. (c) Reactive power. (d) Voltage E. (e) Amplitude of grid voltage.

behave as a weak grid. For the experimental inverter, the settings are the following.

1) The real power $P_{\text{set}} = 200$ W and the reactive power $Q_{\text{set}} = -100$ Var are applied at $t = 5$ s.
2) The real power P_{set} changes to 100 W at $t = 10$ s, and the reactive power Q_{set} changes to -50 Var at $t = 15$ s.
3) At $t = 20$ s, the real power P_{set} returns to 200 W, and the reactive power Q_{set} returns to -100 Var at $t = 25$ s.
4) The test is stopped at $t = 30$ s.

The system responses are shown in the right column of Fig. 5. For the controlled inverter with a simulated weak grid, both frequency and amplitude of grid voltage change with different power settings of the experimental inverter. The grid frequency is less than 60 Hz, because of the positive real power consumption of the resistive load, and the grid voltage is bigger that 110 V_{rms}, because of the negative reactive power consumption of the capacitive load. For the experimental inverter, both real power and reactive power are regulated well in different power settings with fast responses. In each setting change of real power, the grid frequency changes with different real power delivery of the experimental inverter. The experimental inverter frequency follows grid frequency very well, though it has some spikes during the setting changes of real power, it settles down quickly. The setting changes of reactive power also affect the amplitude changes of grid voltage. The experimental inverter

voltage E follows the changes of grid voltage; also, it is affected by the setting change of real power, because of the coupling effects.

The UDE-based control can keep reliable power output regulation in the presence of the disturbances of both frequency and amplitude from the grid voltage. When the grid voltage is changed, the GCI with the UDE-based robust power flow control can regulate the frequency and the voltage of the GCI to follow the changes of the frequency and amplitude from the grid voltage and deliver the required power accurately. This method demonstrates its good low-voltage fault-ride through capability and works well in a weak grid.

D. Comparison With the Active Disturbance Rejection Controller and the Proportional–Integral Controller

To evaluate the good robustness of the UDE-based control, two other controllers, the proportional–integral (PI) controller and another popular robust control, named active disturbance rejection controller (ADRC) [29], are introduced for comparison. The sinusoidal disturbances on both frequency and amplitude of the simulated grid voltage are considered to test their robustness. The system starts with $P_{\text{set}} = 0$ and $Q_{\text{set}} = 0$. Then, we have the following.

1) The real power $P_{\text{set}} = 200$ W and the reactive power $Q_{\text{set}} = -100$ Var are applied at $t = 1$ s.
2) A sinusoidal disturbance $0.2 \cdot \sin(2\pi t)$ Hz is added to the nominal frequency of the grid voltage at $t = 4$ s.
3) At $t = 7$ s, a sinusoidal disturbance $5.5 \cdot \sin(2\pi t)$ V_{rms} is added to the nominal amplitude of the grid voltage.
4) The test is stopped at $t = 12$ s.

For fair comparison, the parameters of three controllers are chosen with similar transient and steady-state performances for step response without disturbances. For ADRC, the following linear extended state observer [29] is adopted for real power control based on the dynamics of real power (5)

$$\begin{aligned} \dot{z}_{p1} &= z_{p2} + \beta_{p1}(y_p - z_{p1}) + \bar{b}_p u_p \\ \dot{z}_{p2} &= \beta_{p2}(y_p - z_{p1}) \end{aligned}$$

where $y_p = P$, z_{p1} is the state estimation of real power P, z_{p2} is the state estimation of lumped uncertain term $\triangle_p$, $\bar{b}_p = \frac{EV_o}{Z_o}$, and u_p is controller output for $\dot{\delta}$. The observer gains are chosen as $\beta_{p1} = 2\omega_{p0}$, $\beta_{p2} = \omega_{p0}^2$, with $\omega_{p0} = 37.7$. The final ADRC law for real power is set as $u_p = [K_p(P_{\text{set}} - y_p) - z_{p2}]/\bar{b}_p$. The ADRC for reactive power can have the same design with $\omega_{q0} = 37.7$. For the PI controller of real power, $k_{\text{pp}} = 0.008$ and $k_{\text{ip}} = 0.06$; the PI controller parameters for reactive power are set as $k_{\text{pq}} = 0.9$ and $k_{\text{iq}} = 6.4$.

The system responses of three methods are shown in both Fig. 6 and Table II. Three methods have similar transient and steady-state performances for step response without disturbance before $t = 4$ s, except that the PI controller has some overshoots on both real power and reactive power. After $t = 4$ s, the UDE-based control has the smaller tracking error of real power than those of ADRC and PI controller as shown in Fig. 6(a). The root mean square (RMS) of real power-tracking error with

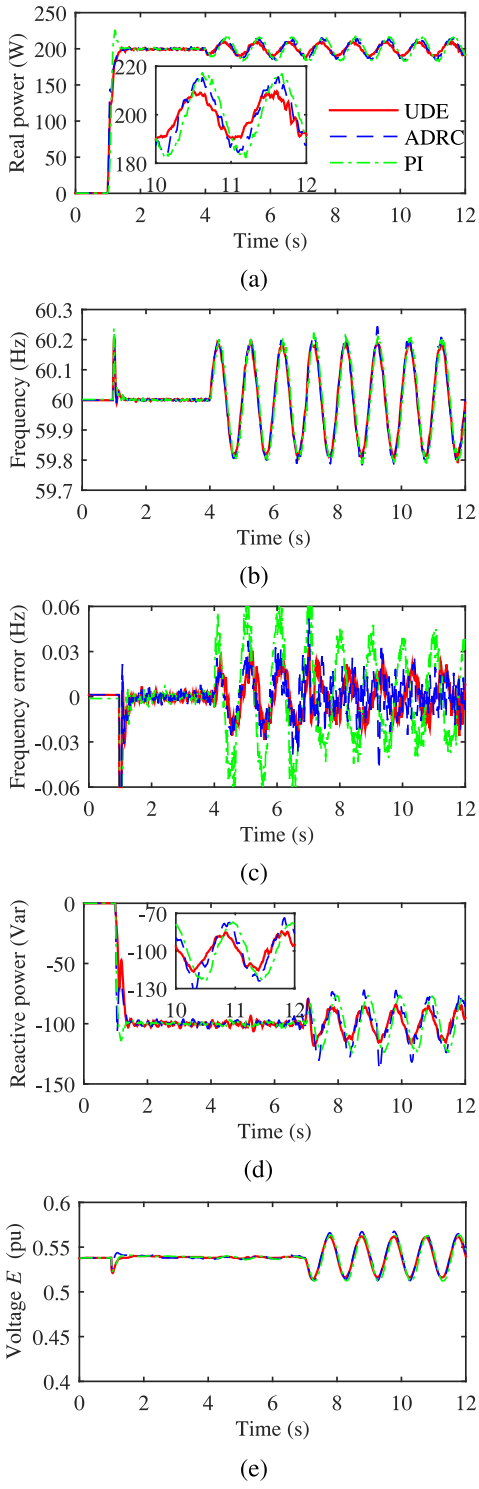

Fig. 6. Comparison of three control methods: UDE-based control, ADRC, and PI controller. (a) Real power. (b) Inverter frequency. (c) Frequency error. (d) Reactive power. (e) Voltage E.

the UDE-based control in steady state (10 s–12 s) is only 6.658 W, which is smaller than that of the ADRC, 10.043 W, and that of the PI controller, 10.466 W, as shown in Table II. Also, the frequency-tracking error between the grid frequency f_g and the inverter frequency f_{inverter} with the UDE-based control is slightly smaller than that of the ADRC and

TABLE II
COMPARISON OF THREE CONTROL METHODS

Conditions		Comparison terms	UDE	ADRC	PI
Transient performance of step response	Real power	Overshoot	0%	0%	13%
		Settling time (s)	0.4	0.4	0.4
	Reactive power	Overshoot	5%	6.5%	14%
		Settling time (s)	0.45	0.45	0.45
Steady-state performance	Without disturbances (2—4 s)	The RMS of real power-tracking error $(e_p)_{\text{rms}}$ (W)	0.812	0.900	0.839
		The RMS of reactive power-tracking error $(e_q)_{\text{rms}}$ (Var)	1.336	1.474	1.409
	With disturbances (10—12 s)	The RMS of real power-tracking error $(e_p)_{\text{rms}}$ (W)	6.658	10.043	10.466
		The RMS of reactive power-tracking error $(e_q)_{\text{rms}}$ (Var)	9.859	15.999	16.097
		The RMS of frequency error $(f_g - f_{\text{inverter}})_{\text{rms}}$ (Hz)	0.0104	0.0124	0.0204

much smaller than that of the PI controller. After $t = 7$ s, the UDE-based control has the smaller tracking error of reactive power compared to the ADRC and PI controller, as shown in Fig. 6(d). The RMS of reactive power-tracking error with the UDE-based control in the steady state (10–12 s) is only 9.859 Var, which is much smaller than that of the ADRC, 15.999 Var, and that of the PI controller, 16.097 Var. Therefore, the UDE-based control has better robustness than the ADRC and PI controller.

V. CONCLUSION

In this paper, an UDE-based robust power flow control has been proposed for GCI to deliver power to the grid accurately. Both frequency dynamics and voltage dynamics were included in the model of power delivery. The UDE algorithm has been adopted for both real power and reactive power control in the presence of model uncertainties, coupling effects, and external disturbances. This method has a simple structure without an extra synchronization unit for the grid-connected operation, and with the easy implementation and parameter tuning. The effectiveness of the proposed approach under different scenarios has been validated experimentally.

ACKNOWLEDGMENT

The authors would like to thank Texas Instruments for the donation of one inverter kit TMDSHV1PHINVKIT.

REFERENCES

[1] Q.-C. Zhong and T. Hornik, *Control of Power Inverters in Renewable Energy and Smart Grid Integration*. New York, NY, USA: Wiley-IEEE Press, 2012.

[2] X. Yuan, F. Wang, D. Boroyevich, Y. Li, and R. Burgos, "DC-link voltage control of a full power converter for wind generator operating in weak-grid systems," *IEEE Trans. Power Electron.*, vol. 24, no. 9, pp. 2178–2192, Sep. 2009.

[3] M. Ashabani and Y. A.-R. I. Mohamed, "Novel comprehensive control framework for incorporating VSCs to smart power grids using bidirectional synchronous-VSC," *IEEE Trans. Power Syst.*, vol. 29, no. 2, pp. 943–957, Mar. 2014.

[4] S. K. Sul, *Control of Electric Machine Drive Systems*. New York, NY, USA: Wiley/IEEE Press, 2011.

[5] M. Prodanovic and T. C. Green, "Control and filter design of three-phase inverters for high power quality grid connection," *IEEE Trans. Power Electron.*, vol. 18, no. 1, pp. 373–380, Jan. 2003.

[6] Z. Liu, J. Liu, and Y. Zhao, "A unified control strategy for three-phase inverter in distributed generation," *IEEE Trans. Power Electron.*, vol. 29, no. 3, pp. 1176–1191, Mar. 2014.

[7] Q.-N. Trinh and H.-H. Lee, "An enhanced grid current compensator for grid-connected distributed generation under nonlinear loads and grid voltage distortions," *IEEE Trans. Ind. Electron.*, vol. 61, no. 12, pp. 6528–6537, Dec. 2014.

[8] D. Jovcic, L. A. Lamont, and L. Xu, "VSC transmission model for analytical studies," in *Proc. IEEE Power Eng. Soc. Gen. Meeting*, Jul. 2003, vol. 3, pp. 1737–1742.

[9] S. M. Ashabani and Y. A.-R. I. Mohamed, "A flexible control strategy for grid-connected and islanded microgrids with enhanced stability using nonlinear microgrid stabilizer," *IEEE Trans. Smart Grid*, vol. 3, no. 3, pp. 1291–1301, Sep. 2012.

[10] M. Ashabani and Y. A.-R. I. Mohamed, "Integrating VSCs to weak grids by nonlinear power damping controller with self-synchronization capability," *IEEE Trans. Power Syst.*, vol. 29, no. 2, pp. 805–814, Mar. 2014.

[11] J.-F. Chen and C.-L. Chu, "Combination voltage-controlled and current-controlled PWM inverters for UPS parallel operation," *IEEE Trans. Power Electron.*, vol. 10, no. 5, pp. 547–558, Sep. 1995.

[12] Q.-C. Zhong, P.-L. Nguyen, Z. Ma, and W. Sheng, "Self-synchronized synchronverters: Inverters without a dedicated synchronization unit," *IEEE Trans. Power Electron.*, vol. 29, no. 2, pp. 617–630, Feb. 2014.

[13] M. C. Chandorkar, D. M. Divan, and R. Adapa, "Control of parallel connected inverters in standalone AC supply systems," *IEEE Trans. Ind. Appl.*, vol. 29, no. 1, pp. 136–143, Jan./Feb. 1993.

[14] M. Dai, M. N. Marwali, J.-W. Jung, and A. Keyhani, "Power flow control of a single distributed generation unit," *IEEE Trans. Power Electron.*, vol. 23, no. 1, pp. 343–352, Jan. 2008.

[15] J. M. Guerrero, J. C. Vasquez, J. Matas, M. Castilla, and L. G. de Vicuna, "Control strategy for flexible microgrid based on parallel line-interactive UPS systems," *IEEE Trans. Ind. Electron.*, vol. 56, no. 3, pp. 726–736, Mar. 2009.

[16] J. Kim, J. M. Guerrero, P. Rodriguez, R. Teodorescu, and K. Nam, "Mode adaptive droop control with virtual output impedances for an inverter-based flexible AC microgrid," *IEEE Trans. Power Electron.*, vol. 26, no. 3, pp. 689–701, Mar. 2011.

[17] W. R. Issa, M. A. Abusara, and S. M. Sharkh, "Control of transient power during unintentional islanding of microgrids," *IEEE Trans. Power Electron.*, vol. 30, no. 8, pp. 4573–4584, Aug. 2015.

[18] F. Nejabatkhah and Y.-W. Li, "Overview of power management strategies of hybrid AC/DC microgrid," *IEEE Trans. Power Electron.*, vol. 30, no. 12, pp. 7072–7089, Dec. 2015.

[19] H.-P. Beck and R. Hesse, "Virtual synchronous machine," in *Proc. 9th Int. Conf. Elect. Power Quality Utilisation*, Oct. 2007, pp. 1–6.

[20] Q.-C. Zhong and G. Weiss, "Synchronverters: Inverters that mimic synchronous generators," *IEEE Trans. Ind. Electron.*, vol. 58, no. 4, pp. 1259–1267, Apr. 2011.

[21] M. A. Torres, L. A. C. Lopes, L. A. Moran, and J. R. Espinoza, "Self-tuning virtual synchronous machine: A control strategy for energy storage

systems to support dynamic frequency control," *IEEE Trans. Energy Convers.*, vol. 29, no. 4, pp. 833–840, Dec. 2014.
[22] L. Zhang, L. Harnefors, and H. P. Nee, "Power-synchronization control of grid-connected voltage-source converters," *IEEE Trans. Power Syst.*, vol. 25, no. 2, pp. 809–820, May 2010.
[23] Q.-C. Zhong and D. Rees, "Control of uncertain LTI systems based on an uncertainty and disturbance estimator," *ASME J. Dyn. Syst., Meas. Control*, vol. 126, no. 4, pp. 905–910, Dec. 2004.
[24] J. P. Kolhe, M. Shaheed, T. S. Chandar, and S. E. Taloe, "Robust control of robot manipulators based on uncertainty and disturbance estimation," *Int. J. Robust Nonlinear Control*, vol. 23, no. 1, pp. 104–122, Jan. 2013.
[25] B. Ren, Q.-C. Zhong, and J. Chen, "Robust control for a class of non-affine nonlinear systems based on the uncertainty and disturbance estimator," *IEEE Trans. Ind. Electron.*, vol. 62, no. 9, pp. 5881–5888, Sep. 2015.
[26] B. Ren, Y. Wang, and Q.-C. Zhong, "UDE-based control of variable-speed wind turbine systems," *Int. J. Control*, 2015, [Online]. Available: http://dx.doi.org/10.1080/00207179.2015.1126678
[27] X. Wang, Y.-W. Li, F. Blaabjerg, and P. C. Loh, "Virtual-impedance-based control for voltage-source and current-source converters," *IEEE Trans. Power Electron.*, vol. 30, no. 12, pp. 7019–7037, Dec. 2015.
[28] Q.-C. Zhong, "Robust droop controller for accurate proportional load sharing among inverters operated in parallel," *IEEE Trans. Ind. Electron.*, vol. 60, no. 4, pp. 1281–1290, Apr. 2013.
[29] Q. Zheng and Z. Gao, "Predictive active disturbance rejection control for processes with time delay," *ISA Trans.*, vol. 53, no. 4, pp. 873–881, Jul. 2014.

Yeqin Wang (S'15) received the B.Eng. degree from the Institute of Technology, China Agricultural University, Beijing, China, in 2009, and the M.Eng. degree from the Clean Energy Automotive Engineering Center, Tongji University, Shanghai, China, in 2012. He is currently working toward the Ph.D. degree at the National Wind Institute, Texas Tech University, Lubbock, TX, USA.

His current research interests include renewable energies and power electronics control.

Beibei Ren (S'05–M'10) received the B.Eng. degree in mechanical and electronic engineering and the M.Eng. degree in automation from Xidian University, Xi'an, China, in 2001 and 2004, respectively, and the Ph.D. degree in electrical and computer engineering from the National University of Singapore, Singapore, in 2010.

From 2010 to 2013, she was a Postdoctoral Scholar with the Department of Mechanical and Aerospace Engineering, University of California, San Diego, CA, USA. Since 2013, she has been an Assistant Professor with the Department of Mechanical Engineering, Texas Tech University, Lubbock, TX, USA. Her current research interests include adaptive control, robust control, distributed parameter systems, extremum seeking, and their applications.

Qing-Chang Zhong (M'04–SM'04) received the Ph.D. degree in control and power engineering from Imperial College London, London, U.K., in 2004 (awarded the Best Doctoral Thesis Prize), and the Ph.D. degree in control theory and engineering from Shanghai Jiao Tong University, Shanghai, China, in 2000.

He is the Max McGraw Endowed Chair Professor in Energy and Power Engineering in the Department of Electrical and Computer Engineering, Illinois Institute of Technology, Chicago, IL, USA.

Prof. Zhong is a Distinguished Lecturer of the IEEE Power Electronics Society and the IEEE Control Systems Society. He is a Fellow of the Institution of Engineering and Technology, U.K., the Vice-Chair of the IFAC Technical Committee on Power and Energy Systems, and was a Senior Research Fellow of the Royal Academy of Engineering, U.K. (2009–2010) and the U.K. Representative to the European Control Association (2013–2015). He serves as an Associate Editor for the IEEE TRANSACTIONS ON AUTOMATIC CONTROL, IEEE TRANSACTIONS ON INDUSTRIAL ELECTRONICS, the IEEE TRANSACTIONS ON POWER ELECTRONICS, IEEE TRANSACTIONS ON CONTROL SYSTEMS TECHNOLOGY, IEEE ACCESS, and the IEEE JOURNAL OF EMERGING AND SELECTED TOPICS IN POWER ELECTRONICS.